

# The link between microscale contact angle measurements and corescale wettability

Chenhao Sun<sup>1</sup>, James McClure<sup>2</sup>, Mehdi, Shabaninejad<sup>3</sup>, Peyman Mostaghimi<sup>1</sup>, Steffen Berg<sup>4</sup> and Ryan T. Armstrong<sup>1,\*</sup>

<sup>1</sup>University of New South Wales, Minerals and Energy Resources Engineering, Sydney, NSW, Australia.

<sup>2</sup>Virginia Polytechnic Institute and State University, Advanced Computing, Blacksburg, Virginia, USA.

<sup>3</sup>Australian National University, Applied Maths, Canberra, ACT, Australia.

<sup>4</sup>Shell Global Solutions International BV, Rock and Fluid Sciences, Amsterdam, The Netherlands.

**Abstract.** Wettability is an important parameter for assessing the performance and optimum recovery scenario for hydrocarbon reservoirs. Relative permeability and capillary pressure-saturation functions show a high sensitivity to wettability. At the core-scale, wettability is defined via the capillary pressure drainage and imbibition cycle, e.g. as Amott-Harvey or USBM indices. At the microscale, the concept of contact angle is used, which until recently was not experimentally possible to determine in a porous rock at reservoir conditions. In this work, the Gauss-Bonnet theorem is used to provide a link between  $Pc(S_w)$  and measured distributions of microscale contact angles. We propose that the wettability of a porous system can be described by geometrical constraints that define the state of immiscible fluids. The constraint describes the range of possible contact angles and interfacial curvatures that can exist for a given system. We present measurements on a sandstone rock for which the USBM index,  $Pc(S_w)$ , and pore-scale contact angles are measured. The results show that pore-scale contact angle measurements can be predicted from capillary pressure data within 4-8% error. This provides a general framework on how petrophysical data can be used to describe the geometrical state of fluids in a porous media.

## 1. Introduction

In a multiphase system, wettability refers to the relative preference between two fluids to coat the solid materials as a consequence of the associated surface energies. This physical consequence is important for special core analysis because it influences relative permeability, end-point saturations, capillary pressure, capillary-end effect and other advanced multiphase flow processes, such as counter-current imbibition [1,2,3,4]. While various laboratory methods can be employed to define the wetting state of a rock there lacks a fundamental framework to incorporate wettability into Darcy scale models. Phenomenological approaches can be applied, such as correlations between Corey exponents and wettability. Common laboratory methods that define wettability are USBM or Amott wettability indices or sessile drop experiments [5]. More recent advances have also allowed for contact angle measurements in a porous rock with fluids at reservoir conditions [6,7]. These measurements bring about an exciting new tool to study the wettability of reservoir rocks. They also raise various fundamental questions regarding the physical meaning and uniqueness of these measurements.

Of particular interest is the link between microscale contact angle and macro-scale wettability indices. Microscale measurements provide the wetting angle

formed between a fluid and solid defined by Young's equation,

$$\sigma_{F_1/S} = \sigma_{F_2/S} + \sigma_{F_1/F_2} \cos \theta \quad (1)$$

where  $\theta$  is the angle formed along the common line in the orthogonal plane when the fluid/solid ( $\sigma_{F_1/S}$ ,  $\sigma_{F_2/S}$ ) and fluid/fluid ( $\sigma_{F_1/F_2}$ ) interfacial tensions are in balance at equilibrium. This measurement is not necessarily practical for macroscale quantification of wettability.

The measurement of  $\theta$  in porous rock requires experiments at reservoir conditions and X-ray computed microtomography imaging followed by a sequence of image processing steps that introduce user-biases and have their own inherent difficulties with precision and accuracy. The measurement is only along the 3-phase common line on the rock surface. The variation of surface roughness and chemical heterogeneity on the rock surface that leads to a wide variation of surface energies is not necessarily quantified adequately. The location of the common line and observed  $\theta$  is dependent on the system parameters. A high versus low capillary number experiment would push the common line into different regions of the pore space. Drainage versus imbibition experiments would produce various distributions of advancing and receding contact angles. Contact angle hysteresis, interface pinning, and the time allotted for the

---

\* Corresponding author: [ryan.armstrong@unsw.edu.au](mailto:ryan.armstrong@unsw.edu.au)

system to reach equilibrium prior to imaging would also influence the observed pore-scale contact angles. Overall, these microscale measurements are an outcome of the dynamical system.

Macroscale indices provide an alternative bulk measurement for porous systems. Methods such as the USBM are based on the drainage and imbibition  $P_c(S_w)$  curves. The USBM provides a single measurement of wettability, which is essentially the ratio of positive to negative work required for saturation. Alternatively, the Leverett J-function can be used to rescale  $P_c(S_w)$  data to match the curve for another rock by adjusting the assigned contact angle given that all other terms are known. This approach would provide a single ‘‘average’’ contact angle for the rock. What these macroscale indices mean in terms of microscale fluid arrangements is unclear.

There currently exists no fundamental link between microscale contact angles and macro-scale wettability indices. Herein, we provide the link by using a theorem from integral geometry that explains the geometrical state of oil clusters in a porous rock in terms of curvature and contact angle. We utilize  $P_c(S_w)$  data to infer the geometrical state of fluid clusters in a sandstone rock to predict the distribution of pore-scale contact angles. This will require an advance review of integral geometry and theorems not commonly applied to porous systems.

### 1.1 Gauss-Bonnet Theorem

The Gauss-Bonnet Theorem [8] can be used to relate the total curvature of an oil cluster ( $C$ ) to its topology ( $\chi$ ),

$$2\pi\chi(\delta C) = \int \kappa_T dA + \int \kappa_g dL \quad (2)$$

where  $\delta C$  is the bounding surface of the cluster,  $dA$  is an area element on the cluster surface,  $\kappa_T = 1/r_1 r_2$  is the Gaussian curvature along the surface,  $r_1$  and  $r_2$  are the two principal radii of curvature at any given location on the surface,  $dL$  is a line element (common line) along the boundary formed by the cluster and solid, and  $\kappa_g$  is the geodesic curvature along  $dL$ . This is an exceptional statement regarding differential surfaces that relates geometry (curvature) to topology (connectivity). The topological term used is the Euler characteristics ( $\chi$ ), which can be decomposed into the number of objects, loops and holes that a given cluster or set of clusters have,

$$\chi(C) = \text{Objects} - \text{Loops} + \text{Holes}. \quad (3)$$

Take for example the bounding surface of a sessile drop, which is a single object with no loops and one hole, resulting in  $\chi(\delta C) = 2$ . There is one hole because we are considering only the bounding surface (manifold) of the droplet not the drop as a solid object. The Euler characteristic for the solid droplet would be  $\chi(C) = 1$  (no holes or loops). The Gauss-Bonnet theorem provides an important link between local geometrical properties and global topological properties, which explains the geometrical state of a bounding surface. Further details on the Gauss-Bonnet theorem and other important aspects of

integral geometry applied to porous systems are provided in a recent review paper [8].

The simplest way to understand the implications of Eq. (2) and its utility for porous systems is to study a sessile drop. We can use piecewise integration for this purpose. The bounding surface,  $A$ , can be partitioned into fluid/fluid and fluid/solid interfaces. There is also a common line separating the two bounding surfaces. Average curvature of the fluid/fluid interface can be defined as  $\kappa_{F1/F2}$  and likewise for the fluid/solid interface  $\kappa_s$ . The geodesic curvature along the common line is defined from two reference planes, i.e. the fluid/fluid interface ( $\kappa_{g_{F1/F2}}$ ) and fluid/solid interface ( $\kappa_{g_{F1/S}}$ ). The latter is the contact angle that is measured during a sessile drop experiment. The former is the angle over which the common line deviates from being straight.

From the previous definitions, we arrive at the following formula,

$$2\pi\chi(\delta C) = A_{F1/S}\kappa_s + A_{F1/F2}\kappa_{F1/F2} + \kappa_g L \quad (4)$$

where  $A_{F1/S}$  is the area between fluid 1 and solid,  $A_{F1/F2}$  is the fluid/fluid area and  $L$  is the length of the common line. The geodesic curvature ( $\kappa_g$ ) of the common line can be partitioned into its curvature components  $\kappa_{g_{F1/S}}$  and  $\kappa_{g_{F1/F2}}$ . Here we assume that  $\kappa_{g_{F1/S}} \gg \kappa_{g_{F1/F2}}$ . The implications of this assumption will be discussed in the results section. The Euler characteristic for the bounding surface of a single droplet is two,

$$\kappa_{g_{F1/S}} = [4\pi - A_{F1/S}\kappa_s + A_{F1/F2}\kappa_{F1/F2}] / L. \quad (5)$$

Eq. 5 explains how contact angle ( $\kappa_{g_{F1/S}}$ ) could change for any homeomorphic deformation of an oil cluster. This is a geometrical constraint. There are no requirements for equilibrium and thus, the result is independent of any force being applied to the droplet and is purely geometrical.

Homeomorphic deformation means that no topological change occurs. Oil droplets that have undergone various homeomorphic deformations are displayed in **Fig. 1**. By inspection it is evident that all of the bounding surfaces are single objects with no loops and one hole. Euler characteristic is the same for all cases despite each having a distinctly different geometrical shape. The implication is that total curvature must be conserved for these droplets, see Eq. 2. For the 2D droplet, the total curvature in the fluid/fluid interface is  $2\pi$  with zero geodesic curvature. For the 2D sessile droplet, the total curvature in the fluid/fluid interface is  $2\pi(1-x)$  where  $x$  is the fraction of the droplet area that is hypothetically extended into the solid substrate. The remaining curvature is in the common points represented by  $\theta$  since the fluid/solid interface is flat with zero curvature. A similar situation occurs for the droplet in a capillary tube. For the dynamic droplet on a decline, the total curvature in the fluid/fluid interface is not trivial and the fluid/solid curvature is zero.

However, the same geometric constraint must apply meaning that any curvature that is not in the fluid/fluid and fluid/solid interfaces must be in the common points representing the advancing and receding contact angles.

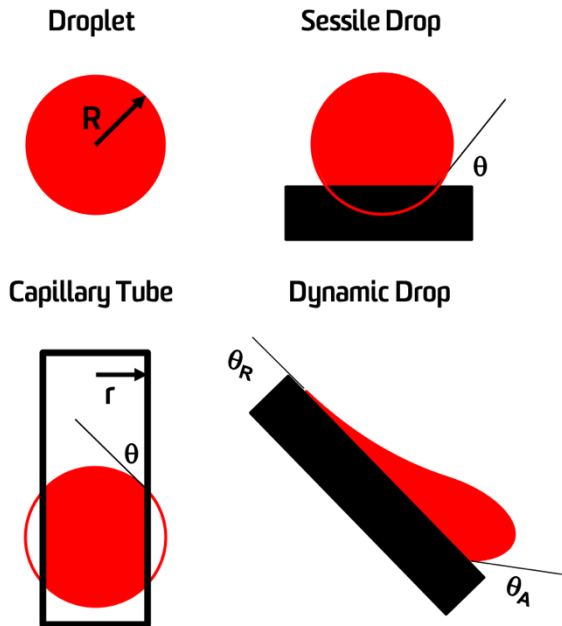


**Fig. 1.** An oil droplet with radius  $R$  (top left) The droplet is placed in a solid surface such that the radius of curvature remains  $1/R$  with contact angle  $\theta$  (top right). The droplet is placed in a capillary tube such that contact angle remains  $\theta$  with radius of curvature  $\cos(\theta)/r$  (bottom left). A droplet moves along a decline with advancing angle  $\theta_A$  and receding angle  $\theta_R$  (bottom right).

An additional example can be provided by considering an oil droplet captured in a microfluidic device, as shown in **Fig. 2**. Here the oil cluster has the same Euler characteristic as the previous examples in **Fig. 1**. The multi-colored curves represent the interfaces. The fluid/fluid interfaces curve outward with positive curvature while the fluid/solid interfaces curve inward with negative curvature. From the segmented image, we cannot resolve the contact of oil with the solid surface. However, regardless of a wetting film existing along the grain surfaces or direct contact of the grains with the solid, the oil always curves away from the solid surface creating negative curvature in regions adjacent to grains. Experimental evidence of this can be found elsewhere [14,15,16,17]. To determine contact we evaluate  $\int \kappa_T dA$  over the multicoloured curves and then subtract the value from  $4\pi$ . The result,  $Re$ , is equal to  $\int \kappa_g dL$ . For the 2D image provided in **Fig. 2**,  $dL$  represents the 20 common points marked by the red stars. The average contact angle (or geodesic curvature) for all common points would be determined by  $Re/20$ .

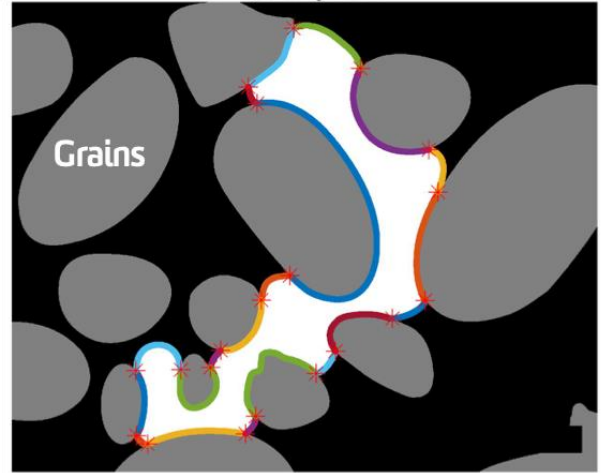


**Fig. 2.** An oil cluster trapped in a microfluidic device. The topology of the cluster is the same as the sessile drops displayed in **Fig. 1**.

## 2. Materials and Methods

We developed a workflow to generate multi-mineral models that can be assigned spatially heterogeneous wetting conditions. These models are used for multiphase flow simulations using the lattice Boltzmann method. A sandstone rock is first imaged with micro-CT followed by impregnation of epoxy and thin sectioning. The thin section is then imaged with Quantitative Evaluation of Minerals by Scanning Electron microscopy, known as QEMSCAN [9]. The analysis provides a high-resolution image of the rock with spatially defined mineral content in 2D. These data are then spatially registered to the 3D micro-CT data [10]. Grey-scale micro-CT values are correlated to mineral content to identify “seed points”. Then sequential sequences of converging active contours are applied by using the seed points as initial positions that advance based on the local image gradient [11]. The final outcome is a segmented 3D image of defined mineralogical information that can be used to assign spatially varying wetting [12]. The workflow is presented in **Fig. 3**.

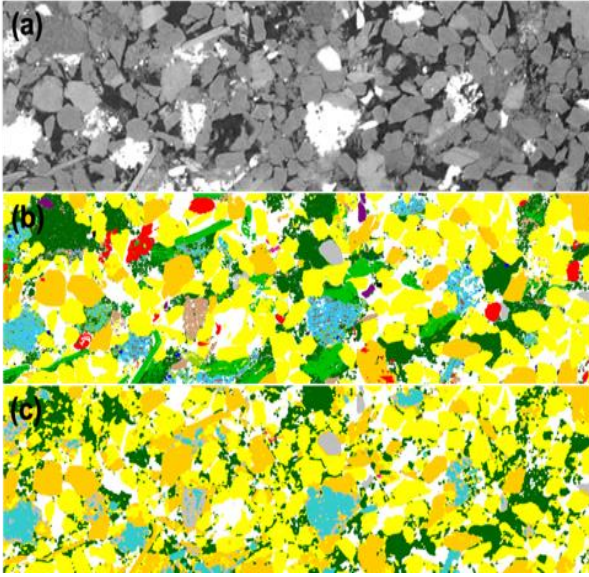


**Fig. 3.** An example of the image processing workflow for generation of the multi-mineral model. Micro-CT image (a), QEMSCAN image (b) and segmented data (c).

We used the 2-phase flow lattice Boltzmann method to simulate drainage and imbibition for various wetting states [12]. Details on the LBM and validation studies are presented elsewhere [13,14,15,16]. We tested two wetting states – one with an overall wettability of 0.1 (neutral wet) and the other with an overall wettability of 0.75 (strongly water wet). Overall wettability,  $W$ , is defined as the summation of the cosine of the contact angles assigned to the mineral surfaces,

$$W = \sum_{i=1}^n \frac{\gamma_{iF1} - \gamma_{iF2}}{\gamma_{F1F2}} \phi_i \quad (6)$$

where  $\gamma$  is interfacial tension with subscripts for each fluid (F) or mineral ( $i$ ) pair and  $\phi_i$  is the solid voxel fraction.

For each  $W$  there were four cases:

- 1) **Homogeneous** - constant wettability everywhere.
- 2) **Corner wet** - corners were water wet, remainder of grain surfaces were oil wet with a constant value.
- 3) **Mineral heterogeneity** - heterogeneous wetting based on the mineral type.
- 4) **Corner wet with mineral heterogeneity** - heterogeneous wetting based on the mineral type, but with water wet conditions applied in the corners.

These cases were designed to mimic commonly assumed conditions for digital rock simulations and/or restored state cores that are aged in crude oil [3,5]. All simulations were initiated from a morphological-based (maximum inscribed spheres) drainage state of  $S_w \sim 0.2$ . Water flooding was simulated until the production curves starts to level off. Once the curves level off at  $\sim 1M$  timesteps, a second set of simulations for secondary drainage were conducted starting from the end-point of the water flood. This provided the hysteretic drainage and imbibition curves required to calculate the USBM index [3]. The phase distributions were then used to measure contact

angles and the curvature of interfaces. For direct contact angle measurements, we used the method explained by [6,7]. This is an apparent contact angle for the visualized fluid clusters. For curvature measurements, we used the approach explained by [17].

### 3. Results and Discussion

Contact angle distributions for the simulations near residual oil saturation are presented in **Figs. 4** and **5**. The corner-wet cases resulted in lower contact angles, which could be characterized as a more water-wet state than the homogeneous and heterogeneous cases. Interestingly the heterogeneous and homogeneous wet cases resulted in similar contact angles distributions and also provided similar  $P_c(S_w)$  curves (data not shown). The largest influence on the pore-scale contact angles appeared to be dictated by the corners and cervices of the rock remaining water wet. This suggests that connate water saturation plays a significant role in the overall observed wettability.

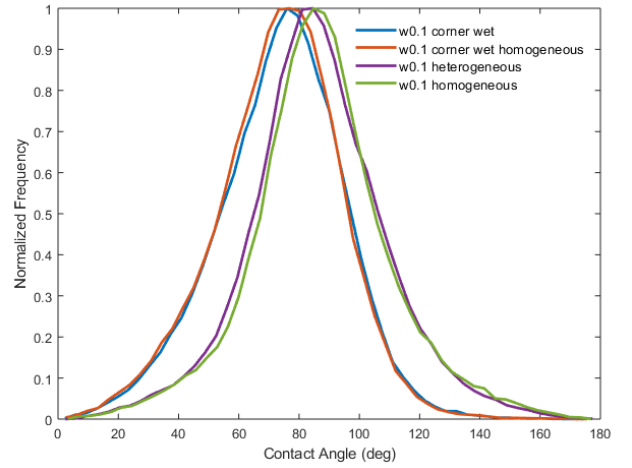


**Fig. 4.** Contact angle distributions for the model systems where the total summation of the cosine of the contact angles for the mineral surfaces are 0.1 (see Eq. 6).

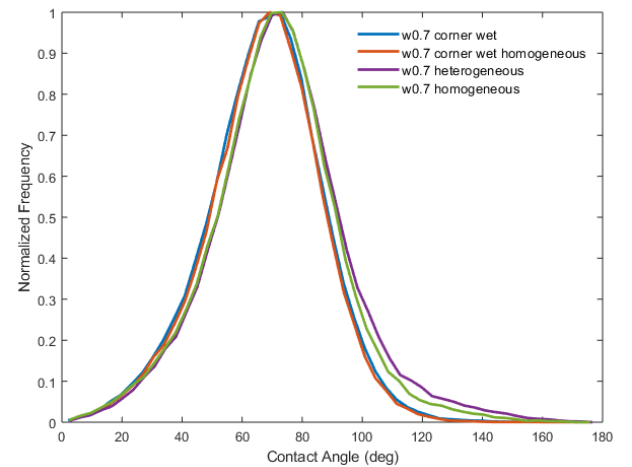


**Fig. 5.** Contact angle distributions for model systems where the total summation of the cosine of the contact angles for the mineral surfaces are 0.7 (see Eq. 6).

For the homogeneous case there was not a unique contact angle with a standard deviation of zero. Indeed, for the homogeneous case, the cosine of the contact angles assigned to each voxel was constant suggesting that the measured contact angle should be constant. A single contact angle was not observed for various reasons. Firstly, the surfaces of the grains are not uniformly smooth, and the direct contact angle measurement does not necessarily account for voxel-by-voxel roughness. The method measures the local angle of the fluid interface and grain surface near the common line by taking a regional approximation [6,7]. The reported values are apparent angles. Secondly, contact angle hysteresis must be considered. During flow there are complex sequences of cooperative dynamics where interfaces are advancing and receding providing a range of various contact angles. Lastly, the measured data was not collected at equilibrium conditions. The data analyzed was collected at residual oil saturation under flowing conditions.

The measured contact angle distributions represent advancing and receding contact angles in addition to local regions where interface could be pinned, such as the entrance to a pore body. Distributions, such as these have been reported for experimental data in carbonate rocks where the surface chemistry is considered to be homogeneous [6]. If or how long it takes an interface to return to its equilibrium condition along the common line after an advancing or receding displacement is an open question. One advantage of using the Gauss-Bonnet theorem to predict the distribution of possible microscale contact angles, as explained later on, is that the methodology is purely geometrical. One also has to keep in mind that using geometric measures probes contact angles within the contact angle hysteresis loop, and not simply the intrinsic contact angle. The outcome therefore provides all of the possible geometrical states for fluid clusters regardless of the underlying dynamics. This applies in particular to techniques assessing contact angles from microscale fluid distributions which are a consequence of flow that are in most cases a superposition of processes with advancing and receding contact lines and various other dynamic effects.

The  $P_c(S_w)$  data for the  $W=0.1$  homogeneous and  $W=0.7$  corner-wet cases are provided in Fig. 6. The simulations were initiated from a morphological-based (maximum inscribed spheres) drainage state of  $S_w \sim 0.2$ . Only the primary imbibition and secondary drainage processes were simulated. The simulation data were also fitted to the Van Genuchten equation to provide a means for determining the USBM index. Connate water saturation was based on the initial state of the simulation, which was determined by the maximum inscribed spheres method. The USBM indices and corresponding contact angle measurements for all of the models are reported in Table 1.

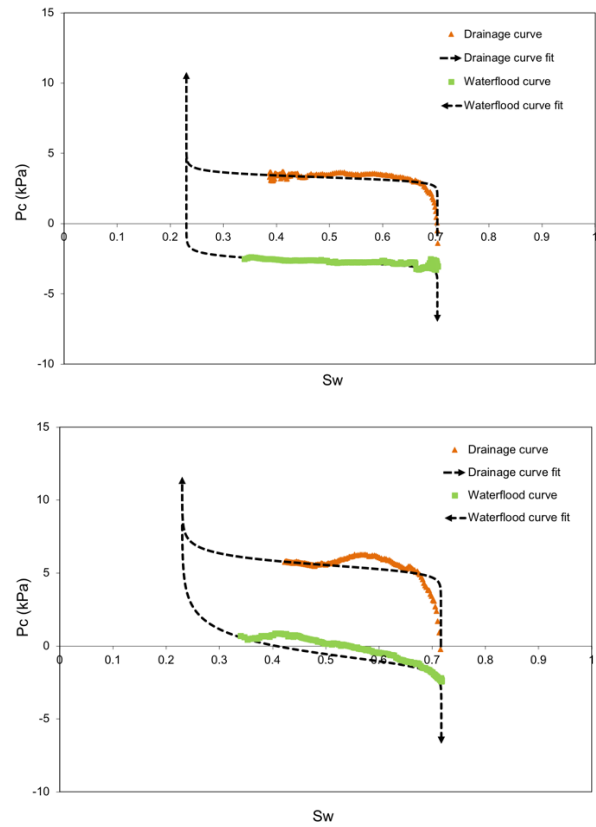


**Fig. 6.** Simulated capillary pressure versus saturation data for the  $W=0.1$  wetting case (top). Simulated capillary pressure versus saturation data for the  $W=0.7$  wetting case (bottom). Regression analysis was used to fit the Van Genuchten equation to the simulated data.

**Table 1.** Summary of pore-scale contact angle measurements and macro-scale USBM wettability indices.

Case	USBM*		Mean $\theta$ (deg)		Standard Deviation (deg)	
	0.1	0.7	0.1	0.7	0.1	0.7
1	0.62	1.00	73.7	67.4	21.0	19.5
2	0.76	0.96	73.0	67.2	20.8	19.0
3	0.19	0.84	86.2	72.9	23.0	22.7
4	0.10	0.88	87.4	70.9	23.4	21.6

USBM indices near 1.0 result in contact angles less than 70 degrees while indices around 0.5 or less result in contact angles greater than 70 degrees. It is interesting that Case 4 with USBM indices of 0.10 and 0.88 resulted in only a 16.5-degree difference in contact angle. The measured contact angles are a sampling of the grain surfaces where the common line exists. The finding is only a statement as to where on the grain surface the common line prefers to be located under the prevailing conditions. We also find that for a single overall wetting

state ( $W$ ) there was variability in the standard deviation of the measured contact angles. Models with more heterogeneous distributions of surface energies resulted in a wider range of contact angles. The trend, however, is minimal because of the previously discussed reasons regarding dynamics, hysteresis and numerical errors that also result in the observed contact angle distributions.

Next, we attempt to predict all of the possible pore-scale contact angles and their associated probabilities for a system of fluid clusters. The prediction is provided by applying a statistical mechanics approach to Eq. 5. First, we define a probability density function for the apparent fluid/fluid curvatures,  $\kappa_{F1/F2}$ , based on  $Pc(Sw)$  data. We assume that a given fluid cluster can be located in any pore region of the rock based on the associated area under the  $Pc(Sw)$  curve. Through the Young-Laplace equation capillary pressure can be related to mean curvature. For axisymmetric interfaces, Gaussian curvature can also be determined since the two principal curvatures are equal. The  $Pc(Sw)$  curve is then divided into local ranges of Gaussian curvatures with associated probabilities.

We consider that an oil cluster of a given volume could be located anywhere in the porous system based on the probability density function of  $\kappa_{F1/F2}$ . Eq. 5 then provides a distribution of possible  $\kappa_{gF1/S}$  for a cluster. The  $\kappa_{gF1/S}$  distributions for each cluster size that spans the entire power law distribution of cluster sizes are then determined. To determine the final distribution for a system of clusters, we then consider the volume distribution of clusters. We combined the distributions of  $\kappa_{gF1/S}$  for individual cluster volumes using a weighted function based on cluster frequency,

$$X_T(i) = \sum w_j x_j(i) \quad (7)$$

where  $x_j(i)$  is the counts for each contact angle  $i$ , and  $w_j$  is the weight for each cluster size  $j$ . Here,

$$w(j) = N_j/N_T \quad (8)$$

where  $N_j$  is the number of clusters of size  $j$  and  $N_T$  is the total number of clusters. The result provides a distribution of apparent  $\kappa_{gF1/S}$  that can be compared to direct pore-scale contact angle measurements presented in **Figs. 4** and **5**.

The predicted and measured contact angle distributions for  $W=0.1$  homogeneous and  $W=0.7$  corner-wet cases are presented in **Figs. 7** and **8**. The results are comparable with less than 4% difference for the average contact angle. We also compare the entire distributions as quantile differences and observe the largest difference of  $\sim 8\%$  for smaller contact angles.

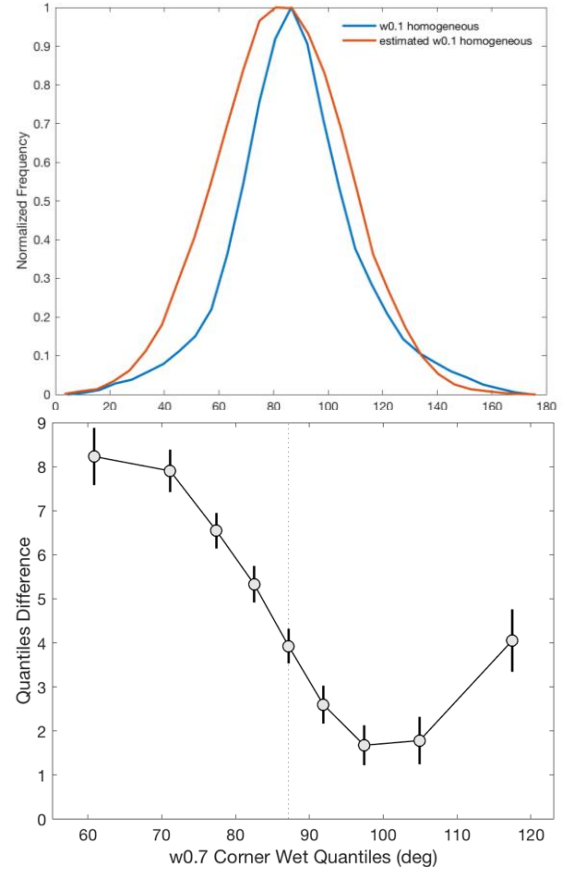


**Fig. 7.** Measured pore-scale contact angles compared to those predicted by Eq. 5 using  $Pc(Sw)$  data (top). Percent differences for each quantile of the contact angle distributions (bottom). The black dashed line represents the mean contact angle.

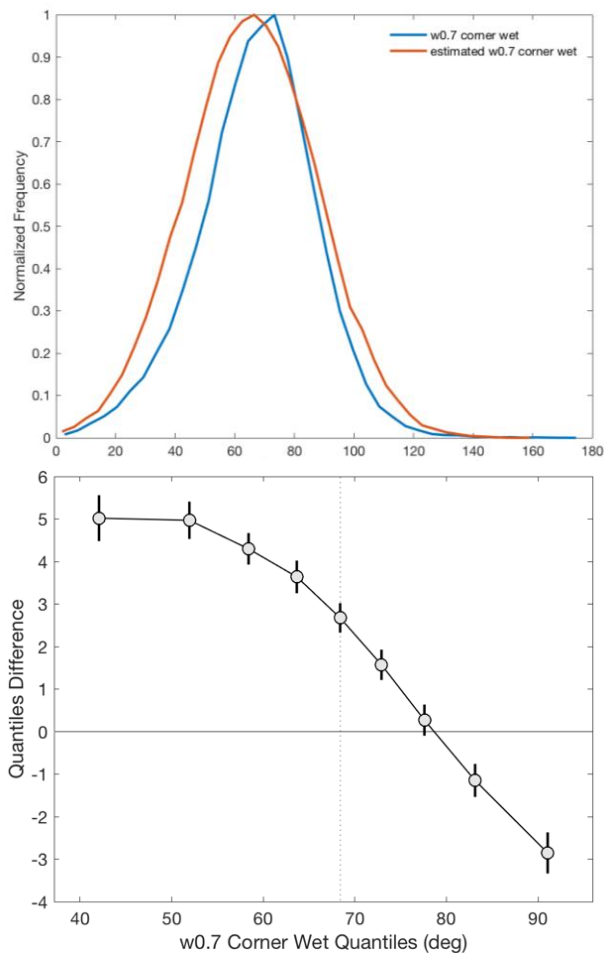


**Fig. 8.** Measured pore-scale contact angles compared to those predicted by Eq. 5 using  $P_c(S_w)$  data (top). Percent differences for each quantile of the contact angle distributions (bottom). The black dashed line represents the mean contact angle.

#### 4. Conclusions

By using the Gauss-Bonnet theorem, we are able to understand how  $P_c(S_w)$  and cluster size distributions are related to the geometrical state of the fluids [8,18]. This provides a direct link between the USBM method measured from  $P_c(S_w)$  data and microscale contact angle measurements. Our predictions of microscale contact angle distributions are within 4% difference for mean contact angle and around 8% difference for the smaller contact angles. The proposed method utilizes two assumptions that could have resulted in these differences. Firstly, we assume that the interfaces in pores are axisymmetric, which is not necessary the case for all porous systems. Secondly, we assume that all clusters could exist in all microscopic states of the porous media. This may occur (open question) at infinite time and space but for our limited observation this is questionable. In addition, it should be noted that the actual pore-scale contact angle measurements also have error and these errors would likely increase for smaller contact angles near rough surfaces. Thus, the assumed benchmark should also be questioned. Despite these issues the results are within a reasonable error margin and the developed framework provides new insights on the geometrical state

of fluids [18] and how core analysis measurements can be used to understand these states [14]. The tested wetting cases demonstrate how the spatial variability of water-wet regions can influence the wetting state of the rock. By using the proposed framework, we can provide a reasonable distribution of microscale contact angles within a dynamical system without the need for direct measurements. These distributions could be used for network models, other modelling approaches, guiding the interpretation of special core analysis results and/or the development of more advanced theories for multiphase flow in porous media.

**Acknowledgements:** This research used resources of the Oak Ridge Leadership Computing Facility, which is a DOE Office of Science User Facility supported under Contract No. DE-AC05-00OR22725. We also thank the members of the ANU/UNSW DigiCore Consortium.

#### References

1. W. G. Anderson, "Wettability literature survey-part 2: Wettability measurement", *Journal of Petroleum Technology*, **38** (11) (1986).
2. W. G. Anderson, "Wettability literature survey part 5: The effects of wettability on relative permeability", *Journal of Petroleum Technology*, **39** (11) (1987).
3. H. Kovscek, C. Wong, A. Radke, "Pore-level scenario for the development of mixed wettability in oil reservoirs", *AIChE Journal* **39** (6) (1993).
4. Donaldson, E. C., Thomas, R. D., Lorenz, P. B. et al., "Wettability determination and its effect on recovery efficiency", *Society of Petroleum Engineers Journal*, **9** (01) (1969).
5. C. McPhee, J. Reed, I. Zubizarreta, "Core analysis: a best practice guide", Vol. 64, *Elsevier* (2015).
6. M. Andrew, B. Bijeljic, M. J. Blunt, "Pore-scale contact angle measurements at reservoir conditions using x-ray microtomography", *Advances in Water Resources*, **68** (2014).
7. A. AlRatrou, A. Q. Raeni, B. Bijeljic and M. Blunt, "Automatic measurement of contact angle in pore-scale images", *Advances in Water Resources*, **109**, 158-269 (2017).
8. R. T. Armstrong, J. McClure, V. Robins, Z. Liu, C. Arns, S. Schlüter, S. Berg, "Porous media characterization using Minkowski functionals: theories, applications and future directions", *Transport in Porous Media*, 1-31 (2018).
9. D. Pirrie, A. R. Butcher, M. R. Power, P. Gottlieb, G. L. Miller, "Rapid quantitative mineral and phase analysis using automated scanning electron microscopy (QEMSCAN); potential applications in forensic geoscience", *Geological Society, London, Special Publications* **232** (1) (2004).

10. S. Latham, T. Varslot, A. P. Sheppard et al., "Image registration: enhancing and calibrating x-ray micro-CT imaging", *Proc. of the Soc. Core Analysts*, Abu Dhabi, UAE (2008).
11. A. P. Sheppard, R. M. Sok, H. Averdunk, "Techniques for image enhancement and segmentation of tomographic images of porous materials", *Physica A: Statistical mechanics and its applications* **339** (1-2) (2004).
12. M. Shabaninejad, J. Middleton, S. Latham, A. Fogden, "Pore-scale analysis of residual oil in a reservoir sandstone and its dependence on water Flood salinity, oil composition, and local mineralogy", *Energy & Fuels*, **31** (12) (2017).
13. J. McClure, J. F. Prins, C. T. Miller, "A novel heterogeneous algorithm to simulate multiphase Flow in porous media on multicore cpu-gpu systems", *Computer Physics Communications* **185** (7) (2014).
14. Z. Liu, J. McClure, R. T. Armstrong, "The influence of wettability on phase connectivity and electrical resistivity", *Physical Review E*, **98** (4) (2018).
15. R. T. Armstrong, J. McClure, M. Berill, M. Rücker, S. Schlüter, S. Berg, "Flow regimes during immiscible displacement", *Petrophysics*, **58** (01) (2017).
16. R. T. Armstrong, J. McClure, M. Rücker, S. Schlüter, M. Berill, S. Berg, "Beyond Darcy's law: The role of phase topology and ganglion dynamics for two fluid flow", *Physical Review E*, **94** (4) (2016).
17. R. T. Armstrong, M. L. Porter and D. Wildenschild, "Linking pore-scale interfacial curvature to column-scale capillary pressure", *Advances in Water Resources*, **46**, 55-62 (2012).
18. J. McClure, R. T. Armstrong, S. Schlüter, M. Berrill, S. Berg, W. Gray, C. T. Miller, "A geometric state function for two-fluid flow in porous media", *Physical Review Fluids*, **3**(8), 084306 (2018).
19. N. R. Morrow, "The effects of surface roughness on contact angle with special reference to petroleum recovery", *The Journal of Canadian Petroleum Technology* 14(04), 42-53, 1975.